SCIENTIFIC REPORTS

OPEN

SUBJECT AREAS:
CARBON NANOTUBES AND FULLERENES
NANOPHOTONICS AND PLASMONICS
ELECTRICAL AND ELECTRONIC ENGINEERING
MATERIALS SCIENCE

Received
27 December 2012

Accepted
31 January 2013

Published
27 February 2013

Correspondence and requests for materials should be addressed to F.L. (fleonar@sandia.gov) or J.K. (kono@rice.edu)

Broadband, Polarization-Sensitive Photodetector Based on Optically-Thick Films of Macroscopically Long, Dense, and Aligned Carbon Nanotubes

Sébastien Nanot[1], Aron W. Cummings[2], Cary L. Pint[3], Akira Ikeuchi[4], Takafumi Akiho[4], Kazuhisa Sueoka[4], Robert H. Hauge[5], François Léonard[2] & Junichiro Kono[1,6]

[1]Department of Electrical and Computer Engineering, Rice University, Houston, TX 77005, USA, [2]Sandia National Laboratories, Livermore, CA 94551, USA, [3]Department of Mechanical Engineering, Vanderbilt University, Nashville, TN 37240, USA, [4]Graduate School of Information Science and Technology, Hokkaido University, Sapporo 060-0814, Japan, [5]Department of Chemistry, Rice University, Houston, TX 77005, USA, [6]Department of Physics and Astronomy, Rice University, Houston, TX 77005, USA.

Increasing performance demands on photodetectors and solar cells require the development of entirely new materials and technological approaches. We report on the fabrication and optoelectronic characterization of a photodetector based on optically-thick films of dense, aligned, and macroscopically long single-wall carbon nanotubes. The photodetector exhibits broadband response from the visible to the mid-infrared under global illumination, with a response time less than 32 μs. Scanning photocurrent microscopy indicates that the signal originates at the contact edges, with an amplitude and width that can be tailored by choosing different contact metals. A theoretical model demonstrates the photothermoelectric origin of the photoresponse due to gradients in the nanotube Seebeck coefficient near the contacts. The experimental and theoretical results open a new path for the realization of optoelectronic devices based on three-dimensionally organized nanotubes.

The photonic and optoelectronic properties of carbon nanomaterials[1,2] have received much attention recently due to their promise for applications in solar technology[3,4] and photodetection[2,5]. In particular, single-wall carbon nanotubes (SWCNTs) are lauded as potential one-dimensional building blocks for constructing photonic devices, components, and systems with tailored optical properties, utilizing their unique ability to emit and/or absorb light at virtually any visible and infrared wavelength through their diameter-dependent optical transitions. Although a number of studies have shown photodetection using single-nanotube devices[6–10], sparse monolayer nanotube arrays[11–13], and random networks of single-wall carbon nanotubes (SWCNTs)[3,4,14–25], large-scale architectures are being sought that fully preserve the unique optoelectronic properties of single nanotubes.

Here we report on the fabrication and optoelectronic characterization of a photodetector based on dense, aligned, macroscopically long, and optically thick SWCNT films. The photodetector exhibits a polarization-sensitive response from the visible to the mid-infrared under global illumination, with a response time less than 32 μs. Scanning photocurrent microscopy indicates that the signal originates at the contact edges, with an amplitude and width that can be tailored by choosing different contact metals. A theoretical model demonstrates the photothermoelectric origin of the photoresponse due to gradients in the nanotube Seebeck coefficient near the contacts.

Results

Vertical lines (height of ~300 μm and thickness of 0.6 μm) of aligned, ultralong SWCNTs were grown by chemical vapor deposition and dry transferred onto SiO_2/Si substrates to make horizontal films[26] (see Supplementary Information). Large metallic electrodes (Au, Pd, or Ti without adhesion layers) were deposited using a shadow mask technique to form two-terminal devices (Fig. 1a–b) with the same or different metals for the two contacts (see Fig. 3 in Supplementary Information), where the current flows parallel or perpendicular to the nanotube orientation. Data were taken using the collimated light of various lasers illuminating the entire device

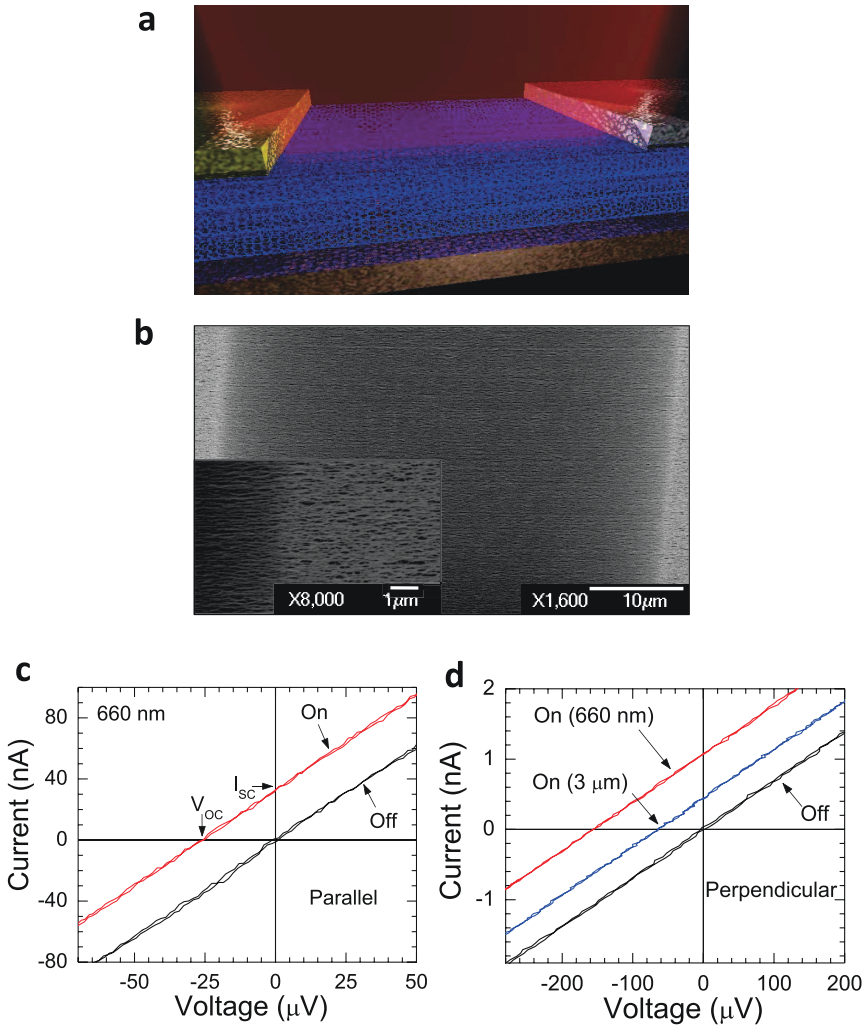

Figure 1 | Carbon nanotube photodetector with macroscopically aligned nanotubes. (a) Schematic of a typical device under global illumination; macroscopically-aligned carbon nanotube films are deposited onto SiO_2 substrates and top contacted with Ti and Pd electrodes. The photoresponse is recorded under monochromatic global illumination. (b) Scanning electron microscope images of a device with two Au electrodes, showing the very high degree of alignment of the nanotubes between the electrodes. (c–d) Current-voltage characteristics in the dark (black line) and under global illumination at 660 nm (red line) for a device where current flows, (c) parallel (power = 60 mW) or, (d) perpendicular (power = 7 mW) to the nanotube orientation. Data for illumination at 3 μm wavelength (power = 55 mW) are also shown.

for global photoresponse and a scanning photocurrent microscopy system to characterize the local photoresponse (see Methods).

The black trace of Fig. 1c represents a typical dark current-voltage characteristic, $I(V)$, obtained at room temperature for an asymmetric device with Ti and Pd contacts, in which the current flows parallel to the nanotubes. The $I(V)$ curve is linear with a resistance of 9 kΩ for this device; two-probe resistance of all measured samples ranged from 80 to 9000 Ω for the parallel configuration and from 3 to 130 kΩ for the perpendicular case (Fig. 1d), depending on the channel length and metal electrodes. Remarkably, under global illumination (Fig. 1c–d), a net photocurrent is generated at zero bias (I_{SC}) as well as an open circuit voltage V_{OC}. This observation is remarkable considering (1) that the I–V curves are not rectifying; (2) the macroscopic size of the devices; and (3) the degree of alignment and density of the SWCNTs.

The photosignal exhibits strong polarization dependence, as shown in Fig. 2a, where I_{SC} is plotted against the angle between the light polarization and the nanotube alignment direction. A signal intensity ratio of ~ ½ is seen between the parallel and perpendicular polarizations with the maximum intensity occurring for the polarization parallel to the nanotubes, independently of the electrode orientation, and including for local illumination over the electrodes. Furthermore, as can be seen from Fig. 2b, the device produces a linear response to visible light (660 nm) as well as near- and mid-infrared light (1.35 to 3.15 μm). Note that the first (second) interband transitions in the semiconducting SWCNTs in these samples occur at ~4 μm (~2 μm) due to their large average diameter (~2.5 nm)[26]. The trace in the main panel of Fig. 2c shows the fast temporal response of the photocurrent under chopped excitation and local illumination. The dashed line is a guide to the eye and corresponds to a time constant of 32 μs limited by the current amplifier. No sign of cut-off is seen up to 6 kHz using a lock-in amplifier (Fig. 2c). This photoresponse is at least two orders of magnitude faster than that reported for other nanotube-film devices[3,24].

Scanning photocurrent microscopy. To understand the origin of the photosignal, we used scanning photocurrent microscopy to measure the spatial dependence of the photoresponse. The results, for a sample with two Au electrodes, are shown in Fig. 3a–b, and indicate strong peaks in the photoresponse at the electrode edges. Such a strong spatial dependence of the photoresponse localized near electrodes has previously been observed in nanotube network devices[17–20,23] and graphene[5,27–32], and has been ascribed to photovoltaic[5,17–20,27–29] or photothermoelectric[24,30–32] effects. Because

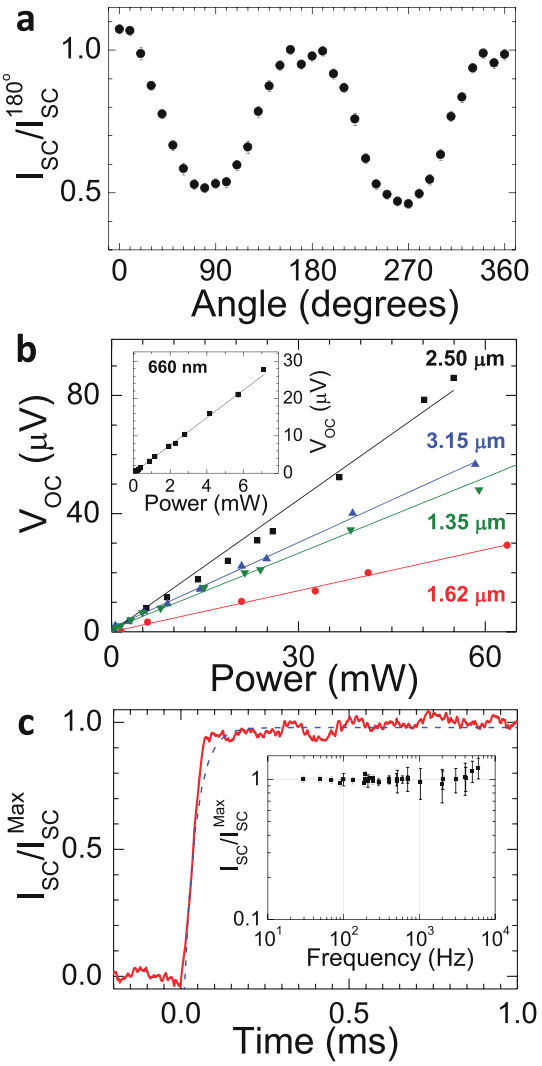

Figure 2 | Polarization-sensitive, broadband, and fast response of the photodetector. (a) Polarization dependence of the photoresponse at 660 nm under local illumination (0° corresponds to the nanotube orientation) for current along the tube axis. Similar results are observed under global illumination and for perpendicular current flow. (b) Linear power dependence of the open-circuit photovoltage at various wavelengths in the mid-infrared range (beam radius of 2.3 mm); **Inset**, photovoltage power dependence under local illumination up to irreversible sample damaging (beam diameter of about 1 μm). (c) Photocurrent time response under chopped excitation and local illumination; the dashed line is a guide to the eye and corresponds to a time constant of 32 μs limited by the current amplifier; **Inset**, frequency dependence of the photoresponse recorded using a lock-in amplifier, which shows no cut-off up to 6 kHz.

different devices can be dominated by either effect depending on their properties[33,34], it is important to understand which mechanism dominates in a given device. To differentiate between the photovoltaic and photothermoelectric mechanisms in our devices, we measured additional devices with different orientations of the SWCNTs and with different contact metals (Ti, Pd, and Au). We find that the width of the signal around the contact edges decreases substantially when current flows perpendicular to the SWCNTs (Fig. 3c). In addition, Ti produces the largest and broadest signal, whereas Pd and Au produce signals of similar amplitude (Fig. 3d). More importantly, all three metals give the same sign for the photoresponse. A polarization ratio around ½ (not shown here), similar to global illumination, is obtained at various positions, and for both current orientations, which indicates that absorption by the SWCNTs plays a direct role in producing the photosignal in all cases.

Modeling. To explain these observations we turn to theory and modeling. We first calculate the band bending in the SWCNT device (see Supplementary Information). Fig. 4a shows the band bending along semiconducting nanotubes for Au or Pd contacts; under the electrodes, the large metal work function leads to charge transfer to the SWCNT film and a large effective p-doping. When combined with the lower p-doping in the channel, a downward band bending away from the electrodes is obtained. This has an immediate consequence for the photovoltaic effect: excitation of electron-hole pairs near the contacts would lead to a positive (negative) photocurrent at the left (right) electrode, in contrast to the experimental observations of Fig. 3. In addition, calculation of the band bending for Ti contacts (Fig. 4b) gives a band bending of the opposite sign compared to Au or Pd; for the photovoltaic effect, this would imply that the sign of the photocurrent should be opposite for Ti compared to the other two metals, which is in disagreement with the experimental results of Fig. 3d. It should also be noted that the width of the signal at the contacts would require a diffusion length of a few microns; based on previously measured recombination times on similar samples[35] this would imply an unlikely mobility of 10^7 cm^2/Vs.

An alternative mechanism is the photothermoelectric effect (PTE). Previous studies considered the PTE at CNT/metal contacts as originating from a thermocouple junction created by the metal electrodes and the CNT film, with a PT voltage between the left and right electrodes given by $V_R - V_L = (S_{CNT} - S_m)(T_R - T_L)$, where S_{CNT} is the Seebeck coefficient of the CNT film, S_m is the Seebeck coefficient of the metal, and $T_R - T_L$ is the temperature difference between the two sides of the system. This simple model has been very useful in establishing the importance of the PTE in nanotube devices[24], but is not sufficient to explain our experimental observations. For example, we find a strong polarization dependence of the PT voltage even for local illumination over the electrodes, which means that light penetrates to the metal/CNT junction; within the simple thermocouple junction model, this would imply that a constant PT voltage should be observed when the laser is over the electrodes and far from the electrode edges. However, the experimental observations in Fig. 3 show that the photovoltage decays to zero in the electrodes. This issue can be resolved by considering the PTE in more detail (see Supplementary Information), leading to the photovoltage

$$\Delta V = -\int_{-\infty}^{\infty} T(x;x_0)\,\frac{dS_{\mathrm{CNT}}}{dx}\,dx, \qquad (1)$$

where x_0 is the position of the laser spot. This model is fundamentally different from the simple thermocouple junction model in that the photosignal depends on the presence of gradients of the Seebeck coefficient in the CNT film, i.e., dS_{CNT}/dx.

To verify the applicability of this model, we combined the band bendings of Fig. 4a–b with a model for the dependence of the Seebeck coefficient of SWCNTs on the position of the Fermi level (Fig. 4c and Supplementary Information; note that changing the maximum value of the Seebeck coefficient in Fig. 4b would only affect the temperature needed to match the experimental data for the photovoltage, and would not qualitatively alter our results). This allows us to obtain $S_{\mathrm{CNT}}(x)$ (Fig. 4d) which then gives $dS_{\mathrm{CNT}}(x)/dx$ (Fig. 4e). This quantity is strongly peaked at the edges of the electrodes due to the localized band bending, *with the same sign* for both Au and Ti. This arises because the opposite sign of the band bending induced by Au and Ti is compensated by a different sign for dS_{CNT}/dE_F because the Au and Ti Fermi levels sit on different sides of the Seebeck peak in Fig. 4c.

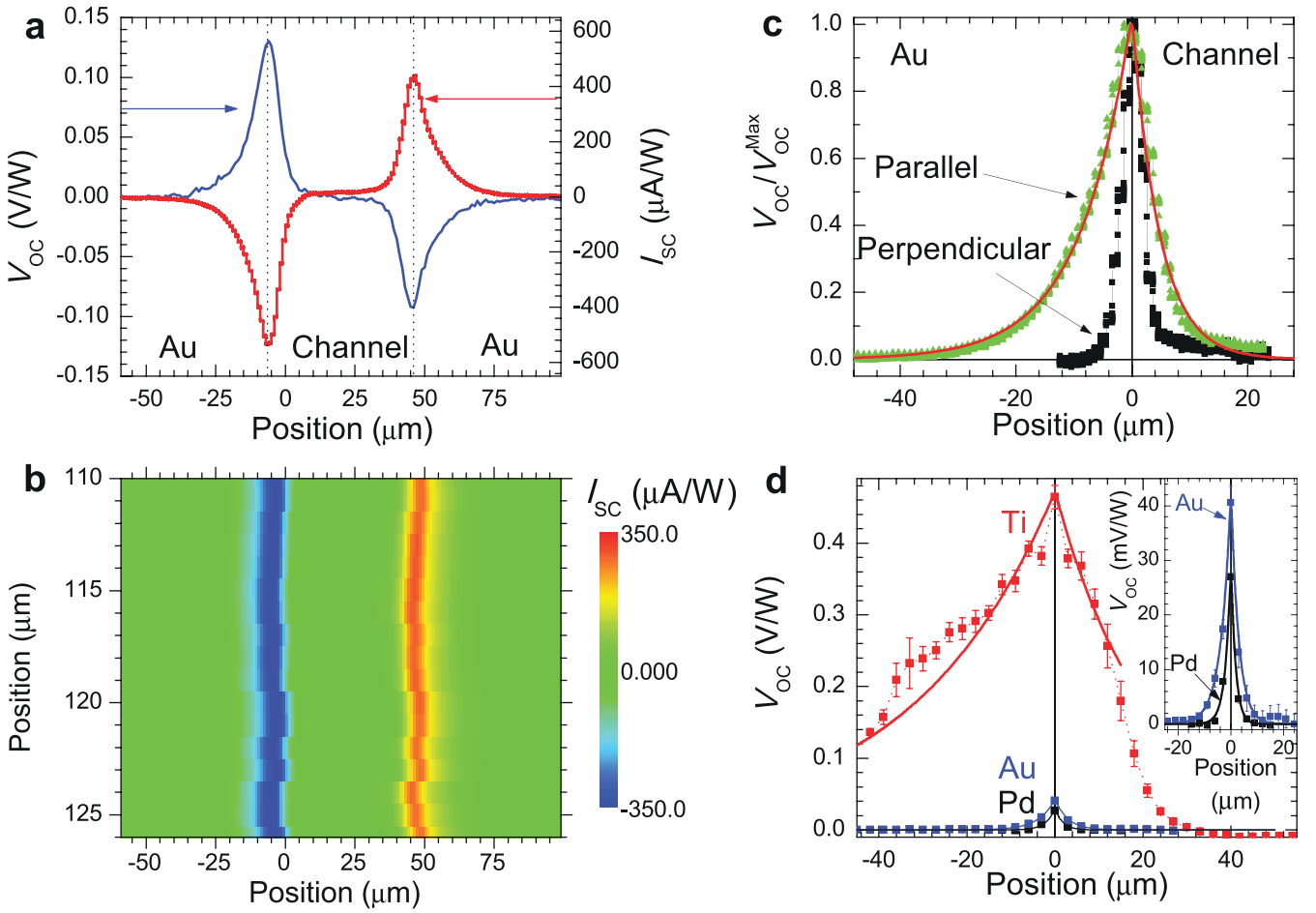

Figure 3 | Scanning photocurrent microscopy. (a) Open circuit photovoltage (blue line, left axis) and short-circuit photocurrent (red line, right axis) show strong maxima and minima at the edges of the electrodes (dashed lines). (b) Photocurrent map shows that the signal is uniform along the width of the sample. (c) Normalized photoresponse for current measurements parallel (▲) or perpendicular (■) to the CNT orientation using the same Au electrode; the red line illustrates a typical fit of the curve using the model discussed in the text. (d) Comparison of the photovoltage near the electrode edges for different metals; data are an average along the length of the contact (error bars correspond to the standard error from averaging). The solid lines are best fits using the model from the text.

To calculate the photovoltage, we also need the temperature. The temperature profile is obtained by considering local heating of the SWCNT film by the laser and heat dissipation in the substrate and the electrodes (Fig. 4f and Supplementary Information); for small laser spot sizes this gives

$$T(x-x_0) = T_{max} e^{-|x-x_0|/\lambda}. \quad (2)$$

The temperature peaks at the position of the laser and decays exponentially with the thermal length scale

$$\lambda = \sqrt{\frac{\kappa h}{G_{eff}}}, \quad (3)$$

where κ is the SWCNT thermal conductivity, h is the film thickness, and G_{eff} is the effective thermal conductance between the SWCNT film and the substrate or the electrodes. Using the values κ = 3000 W/mK[36], h = 0.6 μm, and G_{eff} = 10^8 W/m^{2}K[37], we estimate a thermal length scale of 4 μm. (Note that considering a lower thermal conductivity for short aligned SWCNTs of κ = 200 W/mK[38] would only lower the thermal length scale by a factor of 4, and the estimate for λ would still be in the micron range.).

For a laser spot of finite size, the temperature profile is a convolution of the Gaussian shape of the beam with equation (2); a typical temperature profile for a beam of size 1 micron is illustrated in Fig. 4g for λ = 4 μm. When combined with Fig. 4e (according to equation (1)), it gives a photovoltage that reproduces very well the general behavior of the experimental observations (Fig. 4h). Furthermore, the solid lines in Fig. 3c–d show excellent fits to the experimental data with different values for λ in the channel and under the electrodes. Table 1 shows the extracted values of λ and T_{max} for the different metals and orientations. The values for λ are consistent with the above estimate while the temperature increase is found to be between 0.16 and 4.6 K.

Furthermore, the results show that $\lambda_\perp < \lambda_{//}$, in agreement with equation (3) since $\kappa_\perp < \kappa_{//}$. (For Au contacts, this gives $\kappa_{//}$ 3.2 times larger than $\kappa_\perp$, in good agreement with thermal conductivity measurements in aligned films[38].). We also find that, for the same orientation, both λ and T_{max} are larger for Ti compared with Au or Pd, suggesting that heat transfer to the metal contacts is important and depends on the type of metal. This is consistent with the PTE model because λ and T_{max} both depend inversely on G_{eff}, indicating that G_{eff} is smaller for Ti. The larger λ under the electrodes (e.g., $\lambda_{ch} = 0.79\lambda_{el}$ for Au contacts) is consistent with a model where the laser directly heats the metal, as discussed in the Supplementary Information.

Discussion

Our experiments and modeling show that the different strengths of the PTE at Pd and Ti contacts are responsible for the observation of

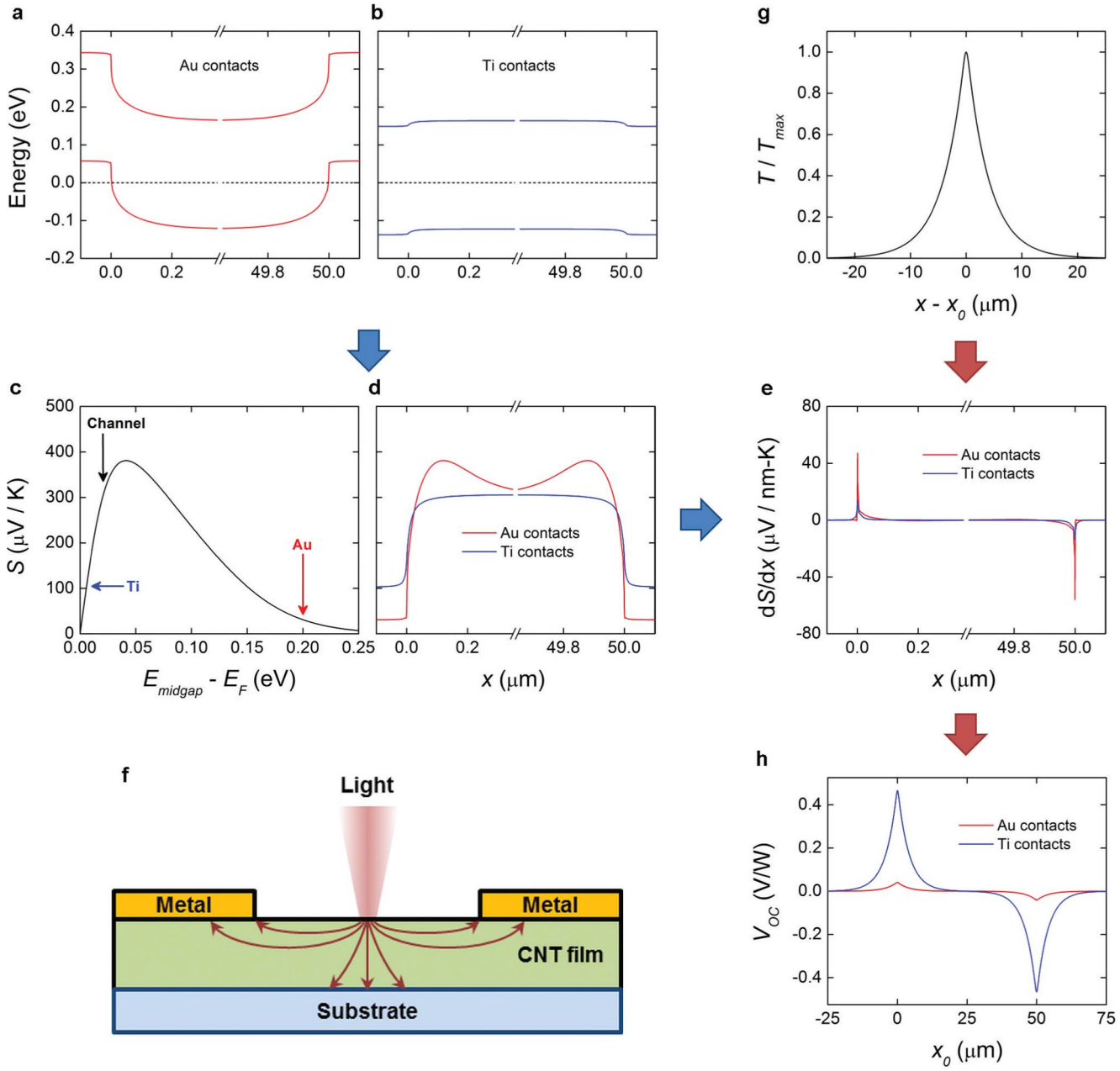

Figure 4 | Theoretical modeling of the carbon nanotube (CNT) photodetector. (a–b) Band-bending along the CNT film with, (a) Au and, (b) Ti contacts. The top curve denotes the conduction band edge, the bottom curve denotes the valence band edge, and the dotted line is the Fermi level. The electrode edges are located at $x = 0$ and $x = 50$ μm. (c) Calculated Seebeck coefficient as a function of the position of the Fermi level with respect to the CNT midgap. The curve is obtained for a (32, 0) CNT. The labels and arrows indicate the value of the Seebeck coefficient in the channel of the CNT film and under each of the contacts. (d) Seebeck coefficient as a function of distance along the CNT film for the band bendings of panels (a) and (b). (e) Derivative of the Seebeck coefficient in (d), indicating strong peaks near the electrode edges. (f) Schematic of the device geometry illustrating the heat conduction paths to the electrodes and the substrate, both contributing to G_{eff}. (g) Illumination causes local heating of the CNT film with a temperature that peaks at the center of the laser spot and decays exponentially over the thermal length scale λ. (h) Calculated photovoltage as a function of the laser spot position, obtained by convoluting the temperature profile as the laser is scanned and the spatial derivative of the Seebeck coefficient. Here, a uniform λ of 4 μm was used with a maximum temperature of 0.29 K for Au contacts and 4.6 K for Ti contacts (see Table 1).

the photoresponse under global illumination in the asymmetric device discussed in Fig. 1. The maximum responsivity of 28 mV/W achieved under visible, global illumination corresponds to a noise equivalent power of ~1.1 10^{-5} W/Hz$^{1/2}$ (at low frequency), and a special detectivity of 4.69 10^3 cm·Hz$^{1/2}$/W (considering the whole area of the device as the active region). While these values are lower than those previously reported for bolometers[16] and CNT-based thermopiles[3], we expect that much larger responses can be ultimately achieved by optimizing the device area and the actual active region, the Seebeck gradient at the contacts, and the thermal management. In addition, the present device response time of 32 μs is about two orders of magnitude faster compared with these previous devices, and the intrinsic response should be even faster. Indeed, from the time-dependent heat conduction equation (see Supplementary Information) the time scale is given by $\tau = h\rho C_p/G_{eff}$. Using $C_p = 600 J/Kg\,K$[39] and the value $\rho = 0.05$ g/cm^3 obtained from mass spectroscopy on our films, we estimate a time response of $\tau = 180$ ns. This underlines that fast photoresponse can be achieved even for

Table 1 | Values for the thermal length and the temperature rise extracted from the experimental data. λ_{ch} and λ_{el} are the thermal length scales and T_{max} is the maximum temperature rise for different metals and orientations

Metal	Orientation	λ_{ch} (μm)	λ_{el} (μm)	T_{max} (K)
Au	Parallel	5.2	6.6	0.16
Au	Perpendicular	2.9	3.7	0.29
Pd	Perpendicular	1.7	2	0.19
Ti	Perpendicular	21	33	4.6

thermal mechanisms, as we observed in our devices. More generally, the results presented here demonstrate that assembly of carbon nanotubes into three-dimensional architectures is a promising path towards novel photonic devices.

Methods

Experimental details. Scanning photocurrent microscopy: The output of a 660-nm laser diode was focused to a diameter of ~1 μm on the sample through a long working-distance apochromatic objective lens with a typical CW power of 2 mW. The sample was kept in vacuum in a microscopy cryostat. An external white light source and a silicon C.C.D. camera were used to optimize the laser beam focusing and positioning on the sample before measurements. The sample was scanned with respect to the excitation spot using two linear stages. At each position we measured either the current-voltage characteristics, $I(V)$ or the open (closed) circuit photovoltage, V_{OC} (photocurrent, I_{SC}) using low-noise preamplifiers. The setup is illustrated in the Supplementary Fig. S3.

Global illumination: Visible and near-infrared excitations were obtained using the collimated beam of laser diodes at 660 nm and 1.35 μm. Mid-infrared excitations were obtained using an optical parametric oscillator, with a module tunable between 1.6 and 1.8 μm (signal) and 2.5 and 3.2 μm (idler). To determine the detectivity, the noise level was determined from measurements of the time dependent current at different cut-off frequencies and was found to be typically one order of magnitude higher than the thermal noise.

Modeling. The band bending along the carbon nanotube device is calculated using a self-consistent non-equilibrium Green's function approach[40]. We simulated a film where 2/3 of the CNTs are (32,0) CNTs and 1/3 are (33,0) CNTs, representing the usual ratio of semiconducting and metallic content in as-grown CNT material. The results presented in the main text are obtained with an intertube spacing of 10.8 nm; the effects of varying the density and composition of the CNT film are discussed in the Supplementary Information. We used a work-function difference of −1 eV (0 eV) between the Pd/Au (Ti) contacts and the nanotubes; charge transfer between the metal and the nanotubes is explicitly included in the simulations, leading to a dipole at the CNT/metal contact and a shift of the CNT bands. We also added a light p-doping of 10^{-5} holes/C-atom to the CNT film. Detailed calculations of the PTE model are provided in the Supplementary Information.

1. Avouris, Ph., Freitag, M. & Perebeinos, V. Carbon-nanotube photonics and optoelectronics. *Nature Photon.* **2**, 341–350 (2008).
2. Bonaccorso, F., Sun, Z., Hasan, T. & Ferrari, A. C. Graphene photonics and optoelectronics. *Nature Photon.* **4**, 611–622 (2010).
3. St-Antoine, B. C., Ménard, D. & Martel, R. Single-walled carbon nanotube thermopile for broadband light detection. *Nano Lett.* **11**, 609–613 (2011).
4. Arnold, M. S. *et al.* Broad spectral response using carbon nanotube/organic semiconductor/C_{60} photodetectors. *Nano Lett.* **9**, 3354–3358 (2009).
5. Mueller, T., Xia, F. & Avouris, P. Graphene photodetectors for high-speed optical communications. *Nature Photon.* **4**, 297–301(2010).
6. Balasubramanian, K., Burghard, M., Kern, K., Scolari, M. & Mews, A. Photocurrent imaging of charge transport barriers in carbon nanotube devices. *Nano Lett.* **5**, 507–510 (2005).
7. Qiu, X., Freitag, M., Perebeinos, V. & Avouris, P. Photoconductivity spectra of single-carbon nanotubes: implications on the nature of their excited states. *Nano Lett.* **5**, 749–752 (2005).
8. Lee, J. U. Photovoltaic effect in ideal carbon nanotube diodes. *Appl. Phys. Lett.* **87**, 073101 (2005).
9. Freitag, M. *et al.* Imaging of the Schottky barriers and charge depletion in carbon nanotube transistors. *Nano Lett.* **7**, 2037–2042 (2007).
10. Gabor, N. M., Zhong, Z., Bosnick, K., Park, J. & McEuen, P. L. Extremely efficient multiple electron-hole pair generation in carbon nanotube photodiodes. *Science* **325**, 1367–1371 (2009).
11. Zeng, Q. *et al.* Carbon nanotube arrays based high-performance infrared photodetector. *Optical Materials Express* **2**, 839 (2012).
12. Chen, C., Lu, Y., Kong, E. S., Zhang, Y. & Lee, S.-T. Nanowelded carbon-nanotube-based solar microcells. *Small* **4**, 1313 (2008).
13. Engel, M. *et al.* Spatially resolved electrostatic potential and photocurrent generation in carbon nanotube array devices. *ACS Nano* **6**, 7303–7310 (2012).
14. Itkis, M. E., Borondics, F., Yu, A. & Haddon, R. C. Bolometric infrared photoresponse of suspended single-walled carbon nanotube films. *Science* **312**, 413–416 (2006).
15. Levitsky, I. A. & Euler, W. B. Photoconductivity of single-wall carbon nanotubes under continuous-wave near-infrared illumination. *Appl. Phys. Lett.* **83**, 1857 (2003).
16. Lu, R., Li, Z., Xu, G. & Wu, J. Z. Suspending single-wall carbon nanotube thin film infrared bolometers on microchannels. *Appl. Phys. Lett.* **94**, 163110 (2009).
17. Lu, S. & Panchapakesan, B. Photoconductivity in single wall carbon nanotube sheets. *Nanotechnology* **17**, 1843 (2006).
18. Merchant, C. A. & Markovic, N. Effects of diffusion on photocurrent generation in single-walled carbon nanotube films. *Appl. Phys. Lett.* **92**, 243510 (2008).
19. Liu, Y., Lu, S. & Panchapakesan, B. Alignment enhanced photoconductivity in single wall carbon nanotube films. *Nanotechnology* **20**, 035203 (2009).
20. Sun, J.-L. *et al.* Photoinduced currents in carbon nanotube/metal heterojunctions. *Appl. Phys. Lett.* **88**, 131107 (2006).
21. St-Antoine, B. C., Ménard, D. & Martel, R. Position sensitive photothermoelectric effect in suspended single-walled carbon nanotube films. *Nano Lett.* **9**, 3503–3508 (2009).
22. Hu, C., Liu, C., Chen, L., Meng, C. & Fan, M. A demo opto-electronic power source based on single-walled carbon nanotube sheets. *ACS Nano* **4**, 4701–4706 (2010).
23. Omari, M. & Kouklin, N. A. Photothermovoltaic effect in carbon nanotubes: En route toward junctionless infrared photocells and light sensors. *Appl. Phys. Lett.* **98**, 243113 (2011).
24. St-Antoine, B. C., Ménard, D. & Martel, R. Photothermolectric effects in single-walled carbon nanotube films: Reinterpreting scanning photocurrent experiments. *Nano Research* **5**, 73 (2012).
25. Prechtel, L., Song, L., Manus, S., Schuh, D., Wegscheider, W, Holleitner, A. W. Time-resolved picoseconds photocurrents in contacted carbon nanotubes. *Nano Lett.* **11**, 269 (2011).
26. Pint, C. L. *et al.* Dry contact transfer printing of aligned carbon nanotube patterns and characterization of their optical properties for diameter distribution and alignment. *ACS Nano* **4**, 1131–1145 (2010).
27. Lee, E. J. H., Balasubramanian, K., Weitz, R. T., Burghard, M. & Kern, K. Contact and edge effects in graphene devices. *Nature Nanotech.* **3**, 486–490 (2008).
28. Park, J., Ahn, Y. H. & Ruiz-Vargas, C. Imaging of photocurrent generation and collection in single-layer graphene. *Nano Lett.* **9**, 1742–1746 (2009).
29. Xia, F. *et al.* Photocurrent imaging and efficient photon detection in a graphene transistor. *Nano Lett.* **9**, 1039–1044 (2009).
30. Gabor, N. M. *et al.* Hot carrier-assisted intrinsic photoresponse in graphene. *Science* **334**, 648–652 (2011).
31. Lemme, M. C. *et al.* Gate-activated photoresponse in a graphene p–n junction. *Nano Lett.* **11**, 4134–4137 (2011).
32. Xu, X., Gabor, N. M., Alden, J. S., van der Zande, A. M. & McEuen, P. L. Photo-thermoelectric effect at a graphene interface junction. *Nano Lett.* **10**, 562–566 (2010).
33. Freitag, M., Low, T., Xia, F. & Avouris, Ph. *Photoconductivity of biased graphene.* arXiv: 1202.5342v1 (2012).
34. Song, J. C. W., Rudner, M. S., Marcus, C. M. & Levitov, L. S. Hot Carrier transport and photocurrent response in graphene. *Nano Lett.* **11**, 4688–4692 (2011).
35. Hashimoto, Y., Murakami, Y., Maruyama, S. & Kono, J. Anisotropic decay dynamics of photoexcited aligned carbon nanotube bundles. *Phys. Rev. B* **75**, 245408 (2007).
36. Pop, E., Mann, D., Wang,Q., Goodson, K. E. & Dai, H. Thermal Conductance of an Individual Single-Wall Carbon Nanotube above Room Temperature. *Nano Lett.* **6**, 96–100 (2006).
37. Pop, E., Mahan, D. A., Goodson, K. E. & Dai, H. Electrical and thermal transport in metallic single-wall carbon nanotubes on insulating substrates. *J. Appl. Phys.* **101**, 093710 (2007).
38. Hone, J. *et al.* Electrical and thermal transport properties of magnetically aligned single-wall carbon nanotube films. *Appl. Phys. Lett.* **77**, 666–668 (2000).
39. Hone, J., Batlogg, B., Benes, Z., Johnson, A. T. & Fisher, J. E. Quantized Phonon Spectrum of Single-Wall Carbon Nanotubes. *Science* **289**, 1730–1733 (2000).
40. Léonard, F. Crosstalk between nanotube devices: contact and channel effects. *Nanotechnology* **17**, 2381–2385 (2006).

Acknowledgements

This work was supported by the US Department of Energy, Office of Science under the National Institute for Nano Engineering (NINE) at Sandia National Laboratories, the Lockheed-Martin Rice University Lancer Program, the National Science Foundation (through Grant Nos. OISE-0968405 and EEC-0540832), the Department of Energy (through Grant No. DE-FG02-06ER46308), and the Robert A. Welch Foundation (through Grant No. C-1509). A.I. and T.A. acknowledge financial support from the Center for Engineering Education Development (CEED) of Hokkaido University.

Author contributions

S.N. fabricated the devices using the carbon nanotubes synthesized by C.L.P. and R.H.H. S.N. performed all the measurements, with assistance by A.I. and T.A., under the guidance of K.S., R.H.H. and J.K. A.C. and F.L. developed the theoretical model and performed the

simulations. All authors contributed to data analysis and interpretation as well as the writing of the manuscript.

Additional information

Supplementary information accompanies this paper at http://www.nature.com/scientificreports

Competing financial interests: The authors declare no competing financial interests.

How to cite this article: Nanot, S. *et al.* Broadband, Polarization-Sensitive Photodetector Based on Optically-Thick Films of Macroscopically Long, Dense, and Aligned Carbon Nanotubes. *Sci. Rep.* **3**, 1335; DOI:10.1038/srep01335 (2013).